

Observational Effects of Anomalous Boundary Layers in Relativistic Jets

M.A. Aloy¹ and P. Mimica¹

Departamento de Astronomía y Astrofísica, Universidad de Valencia, 46100 Burjassot, Spain

MAA, e-mail: Miguel.A.Aloy@uv.es

ABSTRACT

Recent theoretical work has pointed out that the transition layer between a jet and the medium surrounding it may be more complex than previously thought. Under physically realizable conditions, the transverse profile of the Lorentz factor in the boundary layer can be non-monotonic, displaying the absolute maximum where the flow is faster than at the jet spine, followed by an steep fall off. Likewise, the rest-mass density, reaches an absolute minimum (coincident with the maximum in Lorentz factor) and then grows until it reaches the external medium value. Such a behaviour is in contrast to the standard monotonic decline of the Lorentz factor (from a maximum value at the jet central spine) and the corresponding increase of the rest-mass density (from the minimum reached at the jet core). We study the emission properties of the aforementioned anomalous shear layer structures in kiloparsec-scale jets aiming to show observable differences with respect to conventional monotonic and smooth boundary layers.

Subject headings: galaxies: jets: general; X-rays: general — radiation mechanisms: non-thermal; acceleration of particles — methods: numerical; MHD

1. Introduction

The interaction of extragalactic jets with their environment leads, under rather general circumstances, to the stratification of the beam of the jet in the direction normal to its velocity. The morphology of FR I sources (e.g., M87, Owen, Hardee & Cornwell 1989; 3C 31, Laing 1996; 3C 296, Hardcastle, et al. 1997) has been explained in terms of a jet whose dynamics is dominated by a boundary shear layer. In such layers the emissivity in radio and optical maps peaks and, in some cases (e.g., Mrk 501; Cawthorne, et al. 1993), the spectrum

is rather flat, suggesting that the acceleration of non-thermal particles takes place right at the boundary region. Further evidence in favor of such stratification is provided by radio polarization measurements, which indicate that, towards the jet boundary, the magnetic field is highly ordered and parallel to the jet axis (Perlman, et al. 1999).

A radial stratification of jets in FR II radio galaxies has also been observed (Swain, Bridle & Baum 1998; Cawthorne, et al. 1993). The edge brightening found in 3C353 has been interpreted by Swain, Bridle & Baum (1998) as due to the Doppler hiding of the emission of the central spine of the jet, suggesting that most of the observed radiation comes from the jet boundary layer. On the other hand, the *rails of low polarization* found by Swain, Bridle & Baum (1998) close to the jet boundary indicate that the magnetic field in the layer is either axial or toroidal but not radial. Even at parsec scale, the FR II radio jet of 1055+018 exhibits a transverse structure consistent with a *spine - shear boundary layer* jet morphology (Attridge, Roberts & Wardle 1999).

Also sources which are in the borderline dividing FR I and FR II sources show evidences of radial jet stratification. A couple of examples of such sources are 3C 15 and Cen A. In the first case the jet is generally narrower in the optical than in the radio (Dulwich, et al. 2007), and simple spine-sheath model may account for the polarization angle differences seen in the optical and radio data. For Cen A, the recent X-ray data (Kataoka, et al. 2006) can also be properly explained by a stratified jet model with a radially decreasing velocity field.

The aforementioned observational evidence along with some others (e.g., Chiaberge et al. 2000), suggests that the velocity in some jet boundary layers is smaller (but still relativistic) than the velocity of the beam itself. On the other hand, laboratory experiments show that, almost unavoidably, turbulent interaction layers may develop as jets propagate into a viscous medium (e.g., Brown & Roshko 1974). These laboratory shear layers display a radial velocity profile roughly monotonic in which the velocity of the jet core smoothly decreases until it vanishes at the external medium.

From a theoretical point of view, the Reynolds number of the jet flow may reach values of $\sim 10^{23}$ and, hence, it seems unquestionable that such flows will quickly develop a turbulent boundary layer which spreads into the flow and leads to the entrainment and acceleration of ambient gas (De Young 1993). However, the nature and the amount of viscosity in relativistic jets is still largely unknown. Most probably, the effective viscosity in the lateral interaction between the jet and the external medium is a mixture of the turbulent eddy viscosity, magnetic viscosity (based on the finite size of the Larmor radius; see, e.g., Baan 1980) and *cosmic-ray* viscosity (i.e., the viscosity originated due to the diffusion of the momentum carried by energetic particles; see, e.g., Earl, Jokipii & Morfill 1988). Whichever the origin of the viscosity is, the boundary layer itself results from the nonlinear growth of Kelvin-

Helmholtz (KH) instabilities on the jet surface. The fact that relativistic jets are prone to these instabilities was demonstrated theoretically in the pioneer work of Turland & Scheuer (1976). Later, many other papers have explored the stability of relativistic jets with respect to KH instabilities in the vortex-sheet approximation (e.g., Ferrari, Trussoni & Zaninetti 1978; Hardee 1979). Ferrari, Trussoni & Zaninetti (1982) and Birkinshaw (1991) presented the first attempts to study (in the linear regime) the influence of a finite thickness shear layer in classical and relativistic jets, respectively. Very recently, Hardee (2007) has also considered the stability properties (in the linear regime) of spine-sheath magnetized, relativistic jets in which the magnetic field is parallel to the flow velocity. The development of KH modes in sheared relativistic (slab) flows from the linear (analytic) regime to the non-linear regime by means of relativistic hydrodynamic simulations has been carried forward by Perucho, et al. (2007). Alternative approaches to the linear analysis of the stability of stratified relativistic jets and sheared relativistic jets have been performed by Hanasz & Sol (1996), Urpin (2002) Aloy, et al. (2002) and Meliani & Keppens (2007), respectively.

Further support in favor of radial jet stratification as a consequence of the interaction between a jet and its environment is provided by three-dimensional hydrodynamic simulations of relativistic, large scale jets (Aloy et al. 1999a,b,c, 2000a) and two-dimensional simulations of relativistic magnetized jets (Leismann et al. 2005). These simulations show that radially stratified jets are developed out of initially uniform beams. These numerical works display also a rather smooth transition layer with decreasing transverse velocity towards the jet boundary and high specific internal energy. It must be noted that the viscosity in such simulations is of numerical origin, and mimics only qualitatively actual viscous flows.

In addition to the existence of *environmental* reasons to produce a radial flow stratification in astrophysical jets, this effect can also be a natural consequence of the jet formation process. Jet launching from accretion disks may directly lead to a certain mass flux profile and/or magnetic flux profile within the jet. This possibility has been verified by means of axisymmetric MHD simulations both in the classical (Pudridtz, Rogers & Ouyed 2006; Fendt 2006), as well as in the general relativistic (McKinney & Narayan 2007) regime.

Aloy & Rezzolla (2006) show that, under physically plausible conditions (see Sect. 2), the lateral structure of the interaction layer of a relativistic flow can be richer than previously thought. This is also the case in relativistic magnetized jets (Mizuno et al. 2008). Due to a purely relativistic phenomenon (the conversion of specific enthalpy into bulk Lorentz factor across a flow discontinuity), the jet velocity may increase right at the contact discontinuity (CD) separating the jet and the external medium. Beyond the CD the velocity decreases steeply to zero in the radial direction. The growth of the velocity or, equivalently, of the Lorentz factor of the beam is associated to the development of a rarefaction wave that

emerges from the CD where the density and the pressure decrease with respect to their corresponding values at the jet spine. The profiles exhibited by the hydrodynamic variables in these layers are non-monotonic, in contrast with the smooth monotonic profiles that have been typically discussed in the literature. Thereby, we will refer to them as *anomalous* or *AR* shear layers.

As mentioned above, jet shear layers, represent natural sites for particle acceleration, providing high-energy cosmic rays and influencing the dynamics of relativistic jets in extra-galactic radio sources by forming cosmic-ray cocoons (Ostrowski 2000). The efficiency of the acceleration process in these turbulent shear layers depends on the particle mean free path and on the velocity structure. Stawarz & Ostrowski (2002; SO02 hereafter) performed a thorough study of both the acceleration processes acting at jet boundaries and the resulting observational effects. They former authors considered the possibility that turbulent standard boundary layers of kiloparsec scale jets may substantially contribute to the radiative output of the jet. In the present work we will closely follow SO02 working hypothesis, however we will replace the monotonic shear layer kinematic structure they assumed by an anomalous one as suggested by Aloy & Rezzolla (2006). The aim being to show whether AR-shear layers imprint any distinctive feature in the radiation produced by the jet as compared with standard boundary layers. We show in this paper that, indeed, the radiative output of jets bound by anomalous shear layers significantly differs from that of ordinary boundary layers. Thus observations may confirm or rule out the existence of such anomalous shear layers in kiloparsec scale jets and, consistently, this may be used to constrain hardly known physical parameters in these regions.

The plan of the paper is to first show [§ 2] the influence of magnetic fields in the profiles of the physical variables in anomalous boundary layers. In this way we extend the results of Aloy & Rezzolla (2006) and Mizuno et al. (2008) to the adequate parameter range. In Sect. 3 we summarize the basic model developed by SO02 and adapt it to account for the kinematic differences when applied to anomalous shear layers whose profiles will be discussed in Sect. 2. Section 4 provides the spectral energy distribution obtained for the different models of kinematic shear layers shown in the previous section. We discuss our results in Sect. 5 and sum them up in Sect. 5.1.

2. Magnetohydrodynamic boosting in relativistic jet boundary layers

The dynamics of a relativistic magnetohydrodynamic jet in an external medium can be treated as the motion of two fluids, one of which (the jet) is much hotter and at higher (or equal) pressure than the other one (the external medium), and is moving with a large

tangential velocity with respect to the cold, slowly moving fluid. Furthermore, the jet can be magnetized while the external medium magnetic field is much smaller than that of the jet. Aloy & Rezzolla (2006) found that if the specific enthalpy of the jet is sufficiently large, a net conversion of internal to kinetic energy can be produced through a purely relativistic channel. The reason for its exclusively relativistic character is that, the evolution of contact or tangential discontinuities (like, e.g., the one that separates laterally the jet from the external medium), is governed by a genuine coupling between the specific enthalpy and the Lorentz factor at both sides of the discontinuity which does not exist in Newtonian (magneto-)hydrodynamics. Such mechanism yields a substantial hydrodynamic boost along the boundary layer between the jet and the external medium. Basically, the boost along the jet lateral boundaries is due to the work done by the external medium on an overpressured, relativistic jet. Mizuno et al. (2008) extended the validity of the results of Aloy & Rezzolla (2006) to the case in which the jet is magnetized and conclude that the presence of a jet magnetic field (either poloidal or toroidal) enlarges the boost that might be obtained by purely hydrodynamic means. The magnetohydrodynamic boost is larger for jets carrying toroidal than poloidal magnetic fields.

The present analysis is aimed to show what is the qualitative variation of the Lorentz factor and of the magnetic field across a jet boundary layer. Therefore, following Aloy & Rezzolla (2006), we model the interaction between the jet and the external medium as a one dimensional Riemann problem in Cartesian coordinates. Furthermore, we restrict to the case in which the magnetic field is perpendicular to the flow speed in the jet. As demonstrated by Aloy & Rezzolla (2006) and Mizuno et al. (2008) this simple model retains the basic features of the phenomenon. Certainly, a more detailed model would require three dimensional relativistic magnetohydrodynamic simulations.

We solve exactly the Riemann problem set by the jump in the conditions between the jet and the external medium assuming that the magnetic field is perpendicular to the velocity field. For this purpose we use the method devised by Romero et al. (2005). The two uniform “left” (jet) and “right” (external medium) states which set the proposed Riemann problems possess different and discontinuous magnetohydrodynamical properties: the rest-mass density ρ , the total pressure $p = p_{\text{mag}} + p_{\text{gas}}$ (p_{mag} and p_{gas} being the magnetic and the gas pressure, respectively), the components of the velocity normal v^{n} and tangential v^{t} to the initial discontinuity, and the magnetization $\tilde{\beta} := p_{\text{mag}}/p_{\text{gas}}$. In the following, we will use for the quantities in the jet and in the external medium the subscripts “L” and “R”, respectively.

Like in the purely hydrodynamic case, depending on the conditions of the left and right states two qualitatively and quantitatively different solutions develop (Fig. 1). On the one

hand, a pattern of waves can be formed, which we indicate as $\leftarrow \mathcal{S} \mathcal{C} \mathcal{S} \rightarrow$ (Fig. 1 left panel), where $\leftarrow \mathcal{S}$ refers to the shock propagating towards the left sweeping up the jet, $\mathcal{S} \rightarrow$ to the shock moving towards the right crossing the external medium and \mathcal{C} to the contact discontinuity between the two. On the other hand, the pattern can change for sufficiently large velocities parallel to the jet axis (tangential) and in this case the inward-moving shock is replaced by a rarefaction wave thus producing a $\leftarrow \mathcal{R} \mathcal{C} \mathcal{S} \rightarrow$ pattern (Fig. 1 right panel). Once again, we point out that the change in the wave pattern does only happen in relativistic (magneto-)hydrodynamics. Only in the relativistic regime the evolution of a Riemann problem depends upon the components of the velocity parallel to the initial discontinuity or, equivalently, upon the Lorentz factor at both sides of the initial discontinuity. Furthermore, only in the relativistic regime there is a coupling between the momentum and energy fluxes that depends upon the specific enthalpy of initial left and right states.

We notice that the variation of the magnetization in the intermediate left state is less than a few percent when a $\leftarrow \mathcal{R} \mathcal{C} \mathcal{S} \rightarrow$ solution forms (see Fig. 1 right panel). In case a $\leftarrow \mathcal{S} \mathcal{C} \mathcal{S} \rightarrow$ pattern develops, the magnetization in the shocked left intermediate state $\tilde{\beta}_L^*$ grows due to the shock compression, but, in any case, $\tilde{\beta}_L^* \lesssim (2 - 3) \times \tilde{\beta}_L$.

Although Mizuno et al. (2008) have already explored the influence of a dynamically relevant magnetic field in the jet on the aforementioned boost, they restricted their study to only four cases and to extremely hot jets ($p_{\text{gas},L}/\rho_L \geq 10^5$), which is appropriate for gamma-ray burst jets (see, e.g., Aloy, et al. 2000b; Aloy, Janka & Müller 2005; Aloy & Obergaulinger 2007; Birk et al. 2007). Here we consider a parameter space more adequate for kiloparsec scale jets. More precisely, we consider *warm* or *cold* jets with a ratio $p_{\text{gas},L}/\rho_L \leq 10^2$ and a magnetization $\tilde{\beta}_L$, which is varied between 0.1 (slightly magnetized jet) and 10^4 (Poynting flux dominated jet)¹. The left state will have comparable but larger total pressure than the external medium $p_L = 10p_R$, will be under dense $\rho_L/\rho_R = 10^{-5}$, with a fixed bulk Lorentz factor $\Gamma_L \equiv [1 - (v_L^t)^2 - (v_L^n)^2]^{-1/2} = 10$. We choose to fix the external medium (right state) to be cold ($p_R/\rho_R \simeq 10^{-4}$), non-magnetized and non-moving. Precisely, we take for the external medium $p_R = 10^{-6}/\rho_{\text{ext}}c^2$, $\rho_R = 10^{-2}\rho_{\text{ext}}$, $v_R^n = v_R^t = \tilde{\beta}_L = 0$, where ρ_{ext} is a normalization constant which allows us to be scale-free. We point out that with this parametrization we provide physically plausible conditions for both the jet and the external medium. For convenience, hereafter we will assume $c = \rho_{\text{ext}} = 1$, unless stated otherwise.

We explore the resulting Riemann solution as we vary the component of the jet velocity normal to the shear layer² and the jet magnetization $\tilde{\beta}_L$. We point out that models with

¹In Mizuno et al. (2008) a maximum value of $\tilde{\beta}_L = 1.8$ is considered in their model MHDB.

²For a relativistic jet it is expected that such a component is $v_L^n \simeq 0 \ll v_L^t \sim 1$.

$\tilde{\beta} \geq 100$ are actually rather cold, since $p_{\text{gas,L}}/\rho_{\text{L}} \ll 1$ (e.g., for $\tilde{\beta} \geq 10^4$, $p_{\text{gas,L}}/\rho_{\text{L}} \simeq 10^{-2}$). According to the most broadly accepted view, even MHD-generated jets may become matter dominated at kiloparsec scale (e.g., Begelman & Li 1994; Fendt & Ouyed 2004). However, there are others who advocate jet models which are basically electromagnetic entities at such large scales (e.g., Blandford 2002, 2003). In view of these two possible extremes, we have covered the $\tilde{\beta}$ -parameter space with jet models which are both matter dominated and Poynting-flux dominated at kiloparsec scale. In Fig. 2 we show the value of the Lorentz factor reached at the state left to the contact discontinuity Γ_{L}^* . This intermediate state is made out of boosted or deboosted jet matter depending respectively on whether a \mathcal{RCS} , or a \mathcal{SCS} , solution develops.

Figure 2 illustrates how a magnetohydrodynamic boost, where $\Gamma_{\text{L}}^* > \Gamma_{\text{L}}$, exists below a critical value of the normal velocity ($v_{\text{L}}^n \simeq 0.026$ in the case considered here) whereby a \mathcal{RCS} solution develops. The critical value of v_{L}^n is independent of the jet magnetization (note the crossing of all the solutions at the point where $\Gamma_{\text{L}}^* = \Gamma_{\text{L}} = 10$).

The magnetohydrodynamic boost is larger if the magnetization of the jet is increased: while for a poorly magnetized jet ($\tilde{\beta}_{\text{L}} = 0.1$) the boost may increase the bulk Lorentz factor of the layer by $\sim 10\% - 50\%$, for a strongly magnetized jet ($\tilde{\beta}_{\text{L}} \geq 10^2$) the Lorentz factor increase can be $\geq 100\%$. Increasing the magnetization beyond $\tilde{\beta}_{\text{L}} \geq 10^4$ does not produce larger boosts (the effect saturates). Below $\tilde{\beta}_{\text{L}} < 0.1$ the results are almost indistinguishable from the case $\tilde{\beta}_{\text{L}} = 0.1$ and we have decided not to include more lines in the Fig. 2 for the sake of readability.

The bottom line of this parametric study is that for conditions realizable in kiloparsec scale jets, one may find an increase of the Lorentz factor in the transition layer between the jet and the external medium ranging from $(1.5 - 2) \times \Gamma_{\text{L}}$, while the magnetization in that layer is basically the same as in the jet if a \mathcal{RCS} pattern occurs. Furthermore, since only the strength of the magnetohydrodynamic boost, but not its existence, depends on the topology of the field (see Mizuno et al. 2008), we point out that it also happens in the presence of randomly oriented magnetic fields.

3. The physical model

Our model follows very closely that devised by SO02. We assume that non-thermal particles can be accelerated at the boundary layers of relativistic jets (e.g., Ostrowski 1990, 1998, 2000; Rieger & Duffy 2004), thereby producing high-energy cosmic rays. As mentioned in Sect. 1, the main goal of this paper is to replace the prototype shear layer assumed in

SO02 by an anomalous shear layer of the type suggested by Aloy & Rezzolla (2006) and whose basic features have been outlined in Sect. 2. At the most basic level, this means to replace the kinematic shear layer structure assumed by SO02, namely, a jet sheath where the bulk Lorentz factor (Γ) decreases monotonically (Fig. 3a), by a boundary layer where the Lorentz factor develops a spike in which it is larger than at the jet core (Fig. 3b). We shall assume that the magnetic field is uniform in the whole shear layer, which is compatible with the results of our previous section and a reasonable assumption in our simple model.

The working hypothesis made by SO02 are also valid in our case since, the only difference between monotonic and anomalous layers is simply kinematic (see Sect. 3.2). Thus, following SO02, the maximum electron Lorentz factor which can be obtained by the combination of acceleration of particles along the shear layer and the radiative cooling of such particles is

$$\gamma_{\text{eq}} \approx 4 \cdot 10^8 V_8 B_{\mu G}^{-1/2}, \quad (1)$$

where $B_{\mu G}$ is the magnetic field in microgauss and $V_8 \equiv V_A/10^8 \text{ cm s}^{-1}$ is the Alfvén speed V_A in units of 10^8 cm s^{-1} . For kiloparsec scale jets, typical values of these two parameters are $V_8 \simeq 1$ and $B_{\mu G} \sim 10$, which yields $\gamma_{\text{eq}} \simeq 10^8$.

We assume that the resulting spectral energy distribution of the electrons accelerated at the layer consists of a low energy power law $n_e(\gamma) \propto \gamma^{-\sigma}$, with $\sigma = 2$, finished with a high-energy component modeled as a nearly mono energetic peak at $\gamma = \gamma_{\text{eq}}$ due to the pile-up of accelerated particles caused by losses (see Fig. 1 of SO02). In terms of the Dirac delta function, δ , at energies above the injection energy, $\gamma > \gamma_0$, the considered quasy-stationary, averaged spectrum of electrons can be cast in the form

$$n_e(\gamma) = a \gamma^{-\sigma} \exp(-\gamma/\gamma_{\text{eq}}) + b \delta(\gamma - \gamma_{\text{eq}}), \quad (2)$$

where a and b are normalization parameters whose values ($a \simeq 10^{-7} \text{ cm}^{-3}$, $b \simeq 10^{-14} \text{ cm}^{-3}$) result from assuming equipartition between the magnetic field energy density $u_B \equiv B^2 W e / 8\pi$ and the energy densities of both electron spectral components:

$$\int_{\gamma_0}^{\infty} (\gamma m c^2) a \gamma^{-2} \exp(-\gamma/\gamma_{\text{eq}}) d\gamma = \int_{\gamma_0}^{\infty} (\gamma m c^2) b \delta(\gamma - \gamma_{\text{eq}}) d\gamma = \frac{1}{2} u_B. \quad (3)$$

We point out that in SO02, the power-law part of the electron spectrum was also endowed with an exponential cut-off instead of with a Heaviside Θ function in spite of their Eqs. 6 and 7. The Θ function was used in their work only to compute analytic estimates, not for the numerical integrations necessary to calculate their spectral energy distributions (Stawarz 2007).

Assuming equipartition between the particle and magnetic field energy in relativistic sheared jets has been proved to be a rather solid theoretical assumption (see, e.g., Urpin 2006). However, in some cases the values of a and b derived from Eq. 3 and based on equipartition arguments may yield only lower bounds of the true values. Kataoka & Stawarz (2005) argue that powerful jets in quasars and FR II objects can be far from the minimum energy condition, and the field strength very likely exceeds the equipartition value. On the other hand, upper limits to the inverse Compton radiation of the jet in M87 imposed by HESS and HEGRA Cerenkov Telescopes also indicate that the magnetic field cannot be weaker than the equipartition value (Stawarz et al. 2005).

3.1. Radiative processes in boundary layers of kpc-scale jets

The relevant radiative processes taking place at the boundary layer of a relativistic, kpc-scale jet are, on the one hand, the synchrotron (syn) emission of the spectral family represented by Eq. 2 and, on the other hand, their inverse Compton (IC) cooling due to the interaction with the previously produced synchrotron photons (synchrotron self Compton -SSC-) or with seed photons of the cosmic microwave background (external Compton -EC-). These radiative processes are the dominant for large scale relativistic ($\Gamma > 2$) jets at distances from the galactic nucleus $z > 10$ kpc.

Following SO02, we assume that the magnetic field is randomly oriented in the shear layer³. Additionally, we neglect synchrotron self-absorption and, therefore, we limit the computation of the resulting spectra to frequencies $\nu \geq 10^{10}$ Hz.

Restricted to the case of an isotropic electron distribution $n_e(\gamma)$ the synchrotron emissivity averaged over a randomly oriented magnetic field B can be computed from

$$j_{\text{syn}}(\nu) = \frac{\sqrt{3}e^3 B}{mc^2} \int R\left(\frac{\nu}{c_1 \gamma^2}\right) \frac{n_e(\gamma)}{4\pi} d\gamma, \quad (4)$$

where $c_1 = 3eB / 4\pi mc$ and $R(x)$ is a combination of the modified second order Bessel functions (Crusius & Schlickeiser 1986) as

$$R(x) = \frac{x^2}{2} K_{4/3}\left(\frac{x}{2}\right) K_{1/3}\left(\frac{x}{2}\right) - 0.3 \frac{x^3}{2} \left[K_{4/3}^2\left(\frac{x}{2}\right) - K_{1/3}^2\left(\frac{x}{2}\right) \right]. \quad (5)$$

The IC photon emissivity in the source frame⁴, $\dot{n}_{\text{ic}}(\epsilon, \Omega)$, at a certain photon energy ϵ

³Note that anomalous layers can also form if the magnetic field is randomly oriented, see Sect. 2.

⁴In our case the source frame is a cylindrical layer of the boundary region where Γ is assumed to be

(in units of the electron rest mass, $m_e c^2$, $\epsilon \equiv h\nu/m_e c^2$) and scattering direction Ω , is given by

$$\dot{n}_{ic}(\epsilon, \Omega) = c \int d\epsilon_i \oint d\Omega_i \int d\gamma \oint d\Omega_e (1 - \beta \cos \psi) \sigma n_i(\epsilon_i, \Omega_i) n_e(\gamma, \Omega_e), \quad (6)$$

where $n_i(\epsilon_i, \Omega_i)$ is the seed photon number density as a function of the incident photon energy ϵ_i and the photon direction Ω_i , $n_e(\epsilon_e, \Omega_e)$ is the electron energy distribution, ψ is the angle between the electron and the incident photon directions, $\gamma = (1 - \beta)^{1/2}$ is the electron Lorentz factor corresponding to a velocity $v_e = \beta c$ and $\Omega_e = (\cos^{-1} \mu_e, \phi_e)$ its direction in the plasma source frame (e.g., Dermer 1995). The rest-frame emissivity in CGS units is $j_{ic}(\nu, \Omega) = h \epsilon \dot{n}_{ic}(\epsilon, \Omega)$.

In the calculation of the emissivity due to IC process (SSC or EC), we limit ourselves to the Thompson regime, in which the scattering cross section $\sigma \equiv \sigma_T = 6.65 \times 10^{-25} \text{ cm}^2$ is independent of the seed photon energy, which is an adequate approximation in the regime $\gamma \epsilon_i < 1$.

Following Dermer (1995), the scattered photons will be beamed along the direction of the electron motion (i.e. $\Omega \approx \Omega_e$) and will emerge after scattering with an average final energy $\epsilon \approx \frac{4}{3} \gamma^2 \epsilon_{\text{syn}}$. We assume as SO02 that the synchrotron radiation and the electron distribution are isotropic and, therefore, $n_i(\epsilon_i, \Omega_i) = n_{\text{syn}}(\epsilon_{\text{syn}})/4\pi$ and $n_e(\gamma, \Omega_e) = n_e(\gamma)/4\pi$. Then, in Eq. 6 one can use $\sigma = \sigma_T \delta(\Omega - \Omega_e) \delta(\epsilon - (4/3)\gamma^2 \epsilon_{\text{syn}})$ in order to obtain the following expression of $\dot{n}_{\text{SSC}}(\epsilon, \Omega)$:

$$\dot{n}_{\text{SSC}}(\epsilon, \Omega) = \frac{c \sigma_T}{4\pi} \int_0^\infty d\epsilon_{\text{syn}} \int_{\gamma_0}^\infty d\gamma n_{\text{syn}}(\epsilon_{\text{syn}}) n_e(\gamma) \delta \left(\epsilon - \frac{4}{3} \gamma^2 \epsilon_{\text{syn}} \right). \quad (7)$$

Using Eqs. 2, 7, the relation $j_{\text{SSC}}(\nu, \Omega) = h \epsilon \dot{n}_{\text{SSC}}(\epsilon, \Omega)$ and the optically thin synchrotron intensity $I_{\text{syn}}(\nu_{\text{syn}}) \equiv j_{\text{syn}} l = (ch/4\pi) \epsilon_{\text{syn}} n_{\text{syn}}(\epsilon_{\text{syn}})$, where l is the emitting region linear size, the integral form of the synchrotron self-Compton emissivity $j_{\text{SSC}}(\nu)$ is written as

$$j_{\text{SSC}}(\nu) = \sigma_T \int_{\gamma_{\text{low}}}^\infty j_{\text{syn}} \left(\frac{3\nu}{4\gamma^2} \right) l \frac{4\gamma^2}{3} n_e(\gamma) d\gamma, \quad (8)$$

where $\gamma_{\text{low}} = \max(\gamma_0, \frac{3}{4}\epsilon)$ is the lower limit imposed by the restriction $\gamma \epsilon_{\text{syn}} < 1$, which guarantees that we stay within the Thompson regime.

The CMB radiation is strongly anisotropic in the source frame which is moving at a bulk Lorentz factor Γ , providing an external source of seed photons which move opposite to the jet direction, i.e., $\psi \simeq \pi$. Thereby, $(1 - \beta \cos \psi) = (1 + \mu_e)$, where $\Omega_e = (\cos^{-1} \mu_e, \phi_e)$

is the direction of the colliding electron in the comoving frame of the shear layer, similarly to what we made for the case of SSC radiation. In the Thomson regime $\sigma = \sigma_T \delta(\Omega - \Omega_e) \delta[\epsilon - \gamma^2 \epsilon_{\text{cmb}}(1 + \mu_e)]$, since the scattered photon energy is $\epsilon = \gamma^2 \epsilon_{\text{cmb}}(1 + \mu_e)$, where ϵ_{cmb} is the energy of the incident CMB photon in units of the electron rest-mass. Hence, Eq. 6 can be cast as

$$\dot{n}_{\text{EC}}(\epsilon, \Omega) = \frac{c\sigma_T}{4\pi} (1 + \mu) \int_0^\infty d\epsilon_{\text{cmb}} \int_{\gamma_0}^\infty d\gamma n_{\text{cmb}}(\epsilon_{\text{cmb}}) n_e(\gamma) \delta[\epsilon - \gamma^2 \epsilon_{\text{cmb}}(1 + \mu)] . \quad (9)$$

In order to compute the EC emissivity produced by the interaction of CMB photons with the power-law part of the electron distribution, we model the CMB field as a monochromatic radiation with photon energies equal to the average value of a thermal black body spectrum (Blumenthal & Gould 1970) but blue-shifted by a factor Γ , i.e., $\epsilon_{\text{cmb}} = \Gamma \langle \epsilon_{\text{cmb}}^* \rangle \equiv 2.7 \times \Gamma k T^* / m_e c^2$, and a number density $n_{\text{cmb}} = \Gamma u_{\text{cmb}}^* / (\langle \epsilon_{\text{cmb}}^* \rangle m_e c^2)$. The value that we adopt for the energy density of the CMB radiation in the rest frame of the CMB is $u_{\text{cmb}}^* = 4 \cdot 10^{-13} \text{ erg cm}^{-3}$. With these approximations, the EC emissivity associated to the power-law part of the electron distribution can be computed analytically

$$\begin{aligned} j_{\text{EC},1}(\nu) &= \frac{c\sigma_T a}{8\pi} u_{\text{cmb}}^* \left(\frac{h}{2.7kT^*} \right)^{1/2} [(1 + \mu)\Gamma]^{3/2} \exp \left[- \left(\frac{\epsilon}{\Gamma(1 + \mu)\langle \epsilon_{\text{cmb}}^* \rangle \gamma_{\text{eq}}^2} \right)^{1/2} \right] \nu^{-1/2} \\ &\text{if } \gamma_0^2 \leq \frac{h\nu}{2.7kT^*\Gamma(1 + \mu)} . \end{aligned} \quad (10)$$

For the monoenergetic electron peak component, we use the exact black body spectrum transformed to the source frame. In this case, the expression of $n_{\text{cmb}}(\epsilon_{\text{cmb}})$ in the boundary layer comoving frame is (see Eq. 2.58 of Blumenthal & Gould 1970)

$$n_{\text{cmb}}(\epsilon_{\text{cmb}}) = 8\pi m_e \left(\frac{m_e c^2 \epsilon_{\text{cmb}}}{h} \right)^2 \left[\exp \left(\frac{\Gamma m_e c^2 \epsilon_{\text{cmb}}}{kT^*} \right) - 1 \right]^{-1} , \quad (11)$$

where k is the Boltzmann constant. Substituting Eq. 11 and $n_e(\gamma) = b\delta(\gamma - \gamma_{\text{eq}})$ into Eq. 9, taking into account that $j_{\text{EC}}(\nu, \Omega) = h\epsilon \dot{n}_{\text{EC}}(\epsilon, \Omega)$ and the restriction imposed by the Thompson regime ($\epsilon_{\text{cmb}} \gamma_{\text{eq}} < 1$), one obtains

$$\begin{aligned} j_{\text{EC},2}(\nu) &= \frac{2h\sigma_T b}{(1 + \mu)^2 c^2 \gamma_{\text{eq}}^6} \left(\exp \left(\frac{\Gamma h\nu}{(1 + \mu)kT^*} \right) - 1 \right)^{-1} \nu^3 \\ &\text{if } \nu \leq \frac{(1 + \mu)\gamma_{\text{eq}} m_e c^2}{h} . \end{aligned} \quad (12)$$

The total EC emissivity is the sum of Eqs. 10 and 12, i.e.,

$$j_{\text{EC}}(\nu) = j_{\text{EC},1}(\nu) + j_{\text{EC},2}(\nu) . \quad (13)$$

3.2. Kinematic model of the shear layer

We model a large scale jet as a uniform cylindrical spine of radius R_c with a Lorentz factor Γ_c followed by a transition layer where the Lorentz factor changes linearly with radius until $r = R_j$, where the flow velocity either becomes zero (similar to the SO02 model) or reaches a maximum from which it abruptly decreases to zero (Figs. 3, 4). For completeness, we also consider a boundary layer where the Lorentz factor is uniform. More explicitly

$$\Gamma_i(r) = \begin{cases} \Gamma_c & r \leq R_c \\ \Gamma_{j,i} + (\Gamma_c - \Gamma_{j,i}) \frac{R_j - r}{R_j - R_c} & R_c < r \leq R_j \\ 1 & r > R_j \end{cases}, \quad (14)$$

where we take $\Gamma_c = 10$ for our reference models. The subscript $i = 1$ labels the case of a monotonic shear layer ($\Gamma_{j,1} = 1$), $i = 2$ represents the case of an anomalous shear layer ($\Gamma_{j,2} = 15$) and $i = 3$ denotes the case of a jet where the boundary layer is uniform and has the same Lorentz factor as the core ($\Gamma_{j,3} = 10$). The kinematic idealization of the case corresponding to an anomalous layer is a rough prototype of the structure displayed by the Lorentz factor when a \mathcal{RCS} solution develops (Fig. 1). We neglect the variation of the magnetic field across the boundary layer because it is rather small (see Sect. 2) and we assume that the magnetic field is uniform and equal to $10 \mu\text{G}$.

In order to properly normalize the emissivity properties of the different jet models, we choose that all the shear layers transport the same kinetic power as the monotonically decreasing one with a jet radius $R_{j,1} = 2 \text{ kpc}$ and a density and pressure equal to the values chosen for the left state of the models shown in Sect. 2. This means that we adjust the external jet radius of the other two cases to $R_{j,2} = 1.25 \text{ kpc}$ and $R_{j,3} = 1.38 \text{ kpc}$. Since, typically, for extragalactic jets, $\rho_{\text{ext}} \sim 10^{-27} - 10^{-24} \text{ g cm}^{-3}$ (Ferrari 1998), the fluxes of mass and of magnetic field in the jet axial direction are

$$\Phi = 3 \cdot 10^{38} \left(\frac{B}{10^{-4} \text{ G}} \right) \left(\frac{R_j}{1 \text{ kpc}} \right)^2 \text{ G cm}^{-2} \quad (15)$$

$$\dot{M} = 9 \cdot 10^{25} \left(\frac{R_c}{1 \text{ kpc}} \right)^2 \left(\frac{\rho_{\text{ext}}}{10^{-24} \text{ g cm}^{-3}} \right) \text{ g s}^{-1}. \quad (16)$$

For each cylindrical shell in the shear layer of radius r and moving with a bulk Lorentz factor $\Gamma(r)$, we compute the local source frame emissivities for the radiative processes considered in Sect. 3 (Eqs. 4, 8 and 13). Under the assumption that the radiating electrons are distributed uniformly in the boundary layer (for a comoving observer), the emissivity of the sub-layer at the distance r from the jet axis can be computed as

$$j_I^*(\nu^*, \theta^*, r) = \mathcal{D}^2(r, \theta^*) j_I \left(\nu = \frac{\nu^*}{\mathcal{D}(r, \theta^*)}, \mu = \frac{\mu^* - \beta(r)}{1 - \beta(r) \mu^*} \right), \quad (17)$$

where $\mathcal{D}(r, \theta^*) \equiv [\Gamma(r)(1 - \beta(r)\mu^*)]^{-1}$ is the Doppler factor associated to a sub-layer moving with the Lorentz factor $\Gamma(r) = [1 - \beta^2(r)]^{-1/2}$ at an angle $\theta^* \equiv \cos^{-1}\mu^*$ with respect to the line of sight. The subscript $I = \text{syn, SSC or EC}$ specifies the radiative process.

The observed flux density from the boundary layer volume V^* appropriately modified by the flow-beaming patterns is

$$S^*(\nu^*, \theta^*) = d^{-2} \int_{R_{c,i}}^{R_{j,i}} dV^* j^*(\nu^*, \theta^*, r), \quad (18)$$

d being the distance to the observer (we take $d = 10 \text{ Mpc}$ unless stated otherwise). $dV^* = 2\pi\Delta_z r dr$ corresponds to a volume element of the shear layer with an observed length Δ_z , which we assume to be $\Delta_z = 1 \text{ kpc}$. The integrals involved in the evaluation of Eq. 18 are performed numerically and, in order to compute the SSC contribution to the flux density, we estimate the SSC emissivity (Eq. 8) by taking $l = (R_{j,i} - R_{c,i})/\sin\theta^*$.

4. Spectral energy distribution of different models of boundary layers for kpc-scale jets

Our main goal is to outline the observational differences between the emission of large-scale jets laterally endowed by different types of shear layer. The observed spectral energy distribution of the radiation emitted by different kinematic boundary layers in a prototype kpc-scale jet is show in Fig. 5 for two different viewing angles $\theta^* = 1^\circ$ and $\theta^* = 60^\circ$. We neglect both the absorption of very high energy (VHE) gamma-rays during the propagation to the observer and any contribution from a separate non-thermal electron population accelerated at shocks happening at the jet core. The choice of a small and large viewing angle is motivated by the fact that for small viewing angles, $\theta^* \lesssim 4 \simeq 1/\Gamma_{j,2}$, the larger Doppler boosting provided to the emitted radiation by the larger Lorentz factor in AR layers than in monotonic layers makes the total flux density of the former case also slightly larger (Fig. 5 left panel). The differences in the total flux density are smaller in the synchrotron dominated part of the spectrum than in the EC dominated one. At larger angles (Fig. 5 right panel), the flux density predicted for standard layers is 2 to 5 orders of magnitude larger than for uniform or AR layers due to the Doppler hiding of the later two cases. The differences are very important in the EC dominated part of the spectrum (i.e., in the gamma-ray regime).

Both, anomalous and uniform boundary layers generate a rather similar spectral pattern, particularly at small viewing angles. As we observe the jet at larger values of θ^* (Fig. 5 right panel) the smallest Lorentz factor of the uniform case provides a smaller Doppler hiding which results into a larger flux density than in case of AR layers.

Considering specifically the flux density produced by anomalous layers (Fig. 6), we note two main differences with the standard case studied by SO02. First, the separation of the SSC and EC peaks corresponding to IC emission of the power-law distribution of the electrons (Eq. 2) is larger in the former case. For jets with AR layers the frequency separation between the EC1 and SSC1 peaks grows with increasing viewing angle from less than one order of magnitude ($\theta^* \sim 5^\circ$) to more than two orders ($\theta^* \sim 90^\circ$). In case of jets endowed by standard layers (Fig. 7), the frequency separation between the EC1 and SSC1 peaks also grows with the viewing angle, but much less than in the previous case: the frequency separation between the two peaks is smaller than a factor 8 at $\theta^* = 90^\circ$. If a sufficiently large number of TeV photons were detected, this difference could be used to distinguish between jets with standard and anomalous layers. However, we repeat here the cautionary note of SO02: the spectral energy distributions (SEDs) computed in this paper correspond to the most optimistic scenario, with a highly relativistic jet spine and very efficient acceleration creating electrons with large Lorentz factors up to $\gamma_{\text{eq}} \sim 10^8$. Either smaller values of Γ_c or γ_{eq} would reduce the observed very high energy gamma-ray flux and shift the corresponding peaks to lower energies.

The second most important difference between AR and standard radiating boundary layers is that the exponential decay of the synchrotron spectrum is shifted towards smaller frequencies (delving deeper into the very soft X-ray regime). This has a big impact in the effective X-ray spectral index as we will discuss below.

As noted by Komissarov (1990) and confirmed by SO02, extragalactic jets with a monotonic boundary layer may show a jet-to-counterjet radio-to-optical brightness ratio ($S_{\text{syn}}^*(\theta^*)/S_{\text{syn}}^*(\pi - \theta^*)$) which is smaller than if the jet were uniform. We find that such an assertion has to be modified for jets limited by AR-boundary layers. In the latter case, at small viewing angles (namely, $\theta^* \lesssim 5^\circ$ for the considered parametrization) the jet/counterjet asymmetry is $\sim 2 - 3$ times larger than the one corresponding to a uniform jet with the same kinetic power (Fig. 8). At larger viewing angles, the brightness asymmetry turns out to be almost indistinguishable from the case of an equivalent uniform jet (see in Fig. 8 how the solid and dashed lines practically overlap each other for $\theta^* \gtrsim 20^\circ$ if $\Gamma_c = 10$ or for $\theta^* \gtrsim 50^\circ$ in case $\Gamma_c = 3$). Certainly, since the brightness asymmetry is a result of the Doppler boosting (hiding) of the jet (counterjet), the smaller is the value of the maximum Lorentz factor in the anomalous shear layer ($\Gamma_{j,2}$), the smaller will be the maximum asymmetry at small θ^* . If the Lorentz factor of the jet spine is small, the jet-to-counterjet brightness ratio reduces in absolute value (see the grey lines corresponding to $\Gamma_c = 3$, in Fig. 8).⁵ However, even for the

⁵The relative increase of the Lorentz factor in an anomalous shear layer is rather independent on the Lorentz factor of the jet (left state). Therefore, since we have chosen a parametrization for our prototype

relatively small value of $\Gamma_c = 3$ the jet-to-counterjet brightness ratio of the anomalous shear layer case is larger than the one corresponding to the standard case at $\Gamma_c = 10$ independent of the viewing angle (e.g., at $\theta^* = 0^\circ$, $\log [S_{\text{syn}}^*(0)/S_{\text{syn}}^*(\pi)] \simeq 4.35$ for the AR model, while $\log [S_{\text{syn}}^*(0)/S_{\text{syn}}^*(\pi)] \simeq 4.25$). If there were a handle on the value of the Lorentz factor of the jet, this difference might allow us to discriminate observationally between jets with anomalous and standard shear layers. However, given the similarity of the jet-to-counterjet brightness ratio between jets with anomalous layers and jets with *top-hat* profiles (uniform), it might be practically impossible to disentangle from this unique value whether the jet is shielded by an anomalous layer or by no layer at all.

Considering the results obtained for standard boundary layers, SO02 concluded that the mildly relativistic velocities inferred from the observed brightness asymmetries at tens of kiloparsec scales, may correspond to a slower boundary layer and not necessarily to the faster jet core, which might be highly relativistic at the observed distances. If anomalous shear layers may happen in actual jets, slower spines are preferred and relatively moderate maximum shear layer Lorentz factors might also be invoked to explain the observed jet-to-counterjet asymmetries.

In our models, the X-ray radiated power of kpc-scale jets bounded by standard layers is dominated by the high-energy electron bump spectral component, implying that the resulting synchrotron X-ray flux lies above the extrapolated radio-to-optical continuum (see SO02 and Figs. 5, 7). This is also true for jets endowed by anomalous boundary layers (see Fig. 6 at $\nu^* \simeq 10^{17}$ Hz). For both types of layers, the spectral slope at X-ray frequencies may be rather different from that of the power-law at radio-to-optical frequencies, and the difference depends also on the viewing angle. This implies that the effective X-ray spectral index $\alpha_{\text{X,eff}}(\theta^*)$ computed between $h\nu_1^* = 1$ keV and $h\nu_2^* = 5$ keV as

$$\alpha_{\text{X,eff}}(\theta^*) = \frac{\log [S_{\text{X}}^*(\nu_1^*, \theta^*) / S_{\text{X}}^*(\nu_2^*, \theta^*)]}{\log [\nu_2^* / \nu_1^*]}, \quad (19)$$

can be significantly distinct. We point out that $S_{\text{X}}^*(\nu^*, \theta^*)$ is computed in this paper as the value of the flux density calculated using Eq. 18 instead of SO02 who only take $S_{\text{X}}^*(\nu^*, \theta^*) \propto \int r dr \mathcal{D}^2(r, \theta^*) R(x_{\text{eq}}^*)$, with $R(x_{\text{eq}}^*)$ given by Eq. 5, and $x_{\text{eq}}^* = \nu^* / c_1 \gamma_{\text{eq}}^2 \mathcal{D}(r, \theta^*)$.

For highly relativistic jet cores ($\Gamma_c = 10$), Fig. 9 (black lines) shows that the most noticeable difference between jets with anomalous or uniform shear layers and jets with standard limiting boundaries, is the fact that the effective X-ray spectral index of the jet $\alpha_{\text{X,eff}}^j$ is larger than the corresponding to the counterjet $\alpha_{\text{X,eff}}^{\text{cj}}$ for jet inclinations $\theta^* \gtrsim 65^\circ$.

jet in which $\Gamma_{\text{j},2}/\Gamma_c = 1.5$, for the case of $\Gamma_c = 3$ we take $\Gamma_{\text{j},2} = 4.5$.

For standard boundary layer jets $\alpha_{X,\text{eff}}^j \leq \alpha_{X,\text{eff}}^{\text{cj}}$, $\forall \theta^*$ holds (i.e., the counter jet has a steeper X-ray continuum as compared to the jet spectrum). Furthermore, jets with uniform and AR layers show a much larger⁶ jet and counter jet effective X-ray spectral index than jets with standard layers if the inclination is $\theta^* \gtrsim 30^\circ$. Indeed, $\alpha_{X,\text{eff}}^j$ in the former two types of boundary layers is even larger than the $\alpha_{X,\text{eff}}^{\text{cj}}$ corresponding to jets with monotonic layers for viewing angles $\theta^* \gtrsim 30^\circ$.

The large values of the effective X-ray spectral index in jets with uniform and AR layers is due to the fact that the decay of the spectrum after the synchrotron peak crosses the X-ray band and moves towards optical frequencies for inclinations $\theta^* \gtrsim 60^\circ$ (Fig. 6). Consistently, the flux density at 5 keV decays abruptly and, thus $\alpha_{X,\text{eff}}$ grows.

In case of jets with more moderate spine velocities ($\Gamma_c = 3$; Fig. 9, grey lines), there is no viewing angle for which $\alpha_{X,\text{eff}}^j > \alpha_{X,\text{eff}}^{\text{cj}}$, independent on the shear layer model. However, it remains true that the counterjet X-ray spectral index of jets bearing uniform or AR layers is much larger than the one corresponding to standard boundary layer jets (there is a factor of 2 to 4 difference between them).

Taking together the results for models with jet spines flowing at $\Gamma_c = 3$ and 10, it turns out that the range of variability of both $\alpha_{X,\text{eff}}^j$ and $\alpha_{X,\text{eff}}^{\text{cj}}$ is larger for jets flanked by uniform and AR layers than for jets with standard boundary layers. Interestingly, the large-scale X-ray emission observed from several radio-loud AGNs exhibits rather different spectral characteristics. For instance, X-ray spectra of the known jets in quasars are very flat (e.g., $\alpha_X \sim 0.23$ for 3C 207, Brunetti et al. 2001; $\alpha_X \sim 0.5$ for PKS 1127, Siemiginowska et al. 2002; $\alpha_X \sim 0.8$ for 3C 273 and PKS 0637). The low effective spectral index is consistent with small jet inclinations (c.f. Fig. 9, inset) independent of the shear layer model adopted. On the other hand, jets in radio galaxies tend to display relatively steep X-ray spectra, $\alpha_X > 1.0 - 1.5$ (Hardcastle et al. 2001 for 3C 66B, Worrall et al. 2001 for B2 0206 and B2 0755). These values correspond to large inclination angles on Fig. 9, and/or lower jet Lorentz factors for jets with standard boundary layers. But, if uniform or AR emitting layers are considered, the viewing angles needed to account for such values of the X-ray spectral index are smaller ($\theta^* \in [20^\circ, 25^\circ]$ if $\Gamma_c = 10$, or $\theta^* \in [40^\circ, 55^\circ]$ if $\Gamma_c = 3$). Very recently, Hardcastle et al. (2007) have reported values of the X-ray spectral index $\alpha_X > 2.5$ at distances of $\simeq 4$ kpc from the nucleus in Cen A. These large values of α_X are not within reach of jet models flanked by standard layers (the maximum of $\alpha_{X,\text{eff}}^j$ is 1.84 at $\theta^* = 90^\circ$ for the model with $\Gamma_c = 10$). Nonetheless, jets with uniform or AR boundaries may yield $\alpha_{X,\text{eff}}^j > 2.5$ for $\theta^* > 32^\circ$ ($\theta^* > 59^\circ$) if $\Gamma_c = 10$ ($\Gamma_c = 3$). Indeed, considering that the

⁶Particularly, in the range $\theta^* \in [60^\circ, 90^\circ]$, $\alpha_{X,\text{eff},(\text{Uniform,AR})}^j$ is 6 to 7 times larger than $\alpha_{X,\text{eff,standard}}^j$.

inclination of Cen A is $\sim 60^\circ - 70^\circ$ (Skibo, Dermer & Kinzer 1994), our results suggest that, if a uniform or an AR emitting boundary layer were responsible for the emission of Cen A at distances from the nucleus $\gtrsim 4$ kpc, small values of the spine Lorentz factor ($\Gamma_c \simeq 3$) are preferred to explain the large values of α_X observed at such scales.

Although very recently deep *Chandra* observations of Cen A (Hardcastle et al. 2007) have provided us with spectra of some counterjet X-ray features, this is not the usual case for large scale counterjets. There are, however, some estimates of the lower limit of the X-ray brightness asymmetry, like e.g., for the 3C 66B (> 25 , Hardcastle et al. 2001), Pictor A (> 15 , Wilson et al. 2001; 6^{+12}_{-2} Hardcastle & Croston 2005), or PKS 1127-145 (> 5 , Siemiginowska et al. 2002). Our model of AR or uniform radiating boundary layer tends to favor larger X-ray brightness asymmetries between the jet and the counterjet. The reason being that the X-ray emission of the jet is dominated by the synchrotron radiation from the monoenergetic, hard ($\gamma = 10^8$) electron component, while the counterjet emission is dominated by the EC radiation of the power-law part of the electron spectrum.

5. Discussion

SO02 chose the parameters of their radiating boundary layers such that they exhibit clearly the main characteristics of their model. We do not repeat here their discussion. Instead, we focus on the discussion of the choice of the new parameters of our model.

SO02 anticipated that the form of the $\Gamma(r)$ radial profile and of the related spatial variation of the acceleration efficiency can significantly influence the beaming pattern and the intensity of the boundary layer emission. We actually have confirmed this point by replacing the monotonically decaying profile of $\Gamma(r)$ by an idealization of the Lorentz factor profile that results from AR boundaries. This results in a different relative normalization of the SSC and EC components presented in Figs. 5-7.

The uniform layer model could be considered as a limiting case of AR layers when $\Gamma_{j,i} \rightarrow \Gamma_c$. Thus, when looking at the plots of the jet-to-counterjet ratio (Fig. 8) or the X-ray effective spectral index (Fig. 9), any model including an AR layer with $\Gamma_{j,i} \in [10, 15]$ (if $\Gamma_c = 10$; black lines in Figs. 8 and 9) or $\Gamma_{j,i} \in [3, 4.5]$ (if $\Gamma_c = 3$; grey lines in Figs. 8 and 9), would display a graph located between the boundaries set by the solid and dashed lines of the corresponding figures. Since the area enclosed by these two line types (solid and dashed) is rather small, it turns out that our choice of the value of $\Gamma_{j,i} = 1.5\Gamma_c$ does not significantly influence the results. More precisely, if for the considered values of Γ_c (3 or 10) we would have picked up any other value of $\Gamma_{j,i} \in [\Gamma_c, 1.5\Gamma_c]$, neither the value of the jet-to-counterjet

brightness ratio, nor α_X , nor even the spectrum would have changed appreciably. Since, keeping all other physical conditions fixed, a decrease of $\tilde{\beta}_L$ yields smaller values of $\Gamma_{j,i}$, the results we obtain shall be qualitatively valid both for magnetized or non-magnetized jets.

The jet-to-counterjet effective X-ray spectral index asymmetry and its angular dependence (Fig. 9) depends on which of the two spectral components at X-ray frequencies dominates: synchrotron radiation of the monoenergetic, high-energy electron component or the EC radiation from low energy electrons ($\gamma \sim 100$). In its turn, the dominance of any of these two processes depends on the exact shape of the electron spectrum at the highest energies, on the viewing angle, on the jet Lorentz factor and on $\Gamma(r)$. Figure 9 serves as an example of the comparative behavior of different boundary layer models (in which all the parameters are the same except $\Gamma(r)$).

5.1. Summary

In this work, we compare the observational signatures imprinted by different kinematic models of shear layers of kiloparsec scale jets on the radiation of ultrarelativistic electrons accelerated at such boundary layers. The (simple) radiative model of a jet boundary layer follows that of SO02. Alternative (more sophisticated) models to compute the boundary layer radiation from multizone models (see, e.g., Mimica et al. 2004, 2005, 2007) will be considered elsewhere. The most important difference among distinct kinematic models is the radial profile of the Lorentz factor $\Gamma(r)$ across the shear layer. We have considered three different profiles. The first one is the usually assumed for large scale jets, namely, a monotonically decaying Lorentz factor profile (as in SO02). The second one is motivated by the results of Aloy & Rezzolla (2006) and Mizuno et al. (2008), namely, a non-monotonic profile where the Lorentz factor reaches a maximum at the limit between the jet and the external medium (AR layer). For completeness, the case of a uniform jet with a sharp edge is considered. The last case can be regarded as a limit of the AR profile when the maximum Lorentz factor in the boundary layer equals the Lorentz factor of the jet spine. Along the way, we have conveniently developed the results of Aloy & Rezzolla (2006) and Mizuno et al. (2008) to include the effects of dynamically important magnetic fields in the parameter range which is adequate for large scale jets. From such development we have obtained and idealized kinematic model of anomalous boundary layers in magnetized extragalactic jets.

Not surprisingly, we find that the jet-to-counter jet brightness ratio at radio frequencies is larger for jets flanked by AR layers than for uniform or standard layers with the same jet core Lorentz factor. This results from the fact that the differences in the radial profile of the velocity field determine the beaming pattern of the boundary layer emission. Thereby,

this effect has to be taken into account when the jet bulk Lorentz factor is inferred from the jet-to-counterjet brightness asymmetry.

The differences between AR and uniform boundary layer jets are small in the framework of our simple model. In practice, these small differences might render their observational distinction very difficult. Comparing these two models with standard radiating boundary layers the differences are much larger. Several independent clues can be used to distinguish (observationally) among them:

1. If a sufficiently large number of TeV photons were detected, it would be possible to distinguish between jets with standard and anomalous layers by looking at the separation of the SSC and EC peaks. The separation between the two peaks is larger for jets with AR or uniform layers.
2. A large jet-to-counter jet brightness ratio (about two orders of magnitude larger than in standard boundary layer jets) is expected for jets bounded by AR or uniform layers.
3. For large viewing angles the effective X-ray spectral index is much larger for AR or uniform jets than for jets with standard boundary layers.
4. There can exist an inversion of the jet and counterjet X-ray spectral indices for jets seen at large viewing angles. However, for most inclination angles and moderate bulk Lorentz factors of the jet core, the effective X-ray spectral index of the jet is much smaller than that of the counterjet. Indeed, if there is a hint on the bulk Lorentz factor of the jet (e.g., because superluminal proper motions are detected), the jet-to-counterjet spectral X-ray index ratio may tell us whether the radiating layer is uniform, standard or AR. We note that for large Lorentz factors of the jet core ($\Gamma_c \lesssim 8$), the largest ratio $\alpha_{X,\text{eff}}^j/\alpha_{X,\text{eff}}^{cj}$ corresponds to jets with uniform layers, whilst the smaller one should be identified with standard boundary layers. For more moderate core Lorentz factor, the ratio $\alpha_{X,\text{eff}}^j/\alpha_{X,\text{eff}}^{cj}$ is larger for jets flanked by AR layers than for jets with uniform or standard layers. In spite of these facts, the differences in the effective spectral X-ray index between models with uniform and with AR layers are rather small and, they might render their observational distinction very difficult unless a very careful analysis of the observational data is performed.

We kindly acknowledge the work of Jerome Ferrand during his internship at the Departamento de Astronomía y Astrofísica. We also thank L. Stawarz for very useful discussions and helpful hints. MAA is a Ramón y Cajal Fellow of the Spanish Ministry of Education and Science. He also acknowledges partial support from the Spanish Ministry of Education and

Science (AYA2004-08067-C03-C01, AYA2007-67626-C03-01, CSD2007-00050). PM is at the University of Valencia with a European Union Marie Curie Incoming International Fellowship (MEIF-CT-2005-021603). The authors thankfully acknowledge the computer resources, technical expertise and assistance provided by the Barcelona Supercomputing Center - Centro Nacional de Supercomputación.

REFERENCES

Aloy, M.A., Ibáñez, J.M., Martí, J.M., Müller, E. 1999, *ApJ Supl. Ser.*, 122, 151

Aloy, M.A., Ibáñez, J.M., Martí, J.M., Gómez, J.L., & Müller, E. 1999, *ApJ*, 523, L125

Aloy, M.A., Pons, J.A., Ibáñez, J.M. 1999, *Comp. Phys. Comm.*, 120, 115

Aloy, M.A., Gómez, J.L., Ibáñez, J.M., Martí, J.M., & Müller, E. 2000, *ApJ*, 528, L85

Aloy, M.A., Müller, E., Ibáñez, J.M., Martí, J.M., & MacFadyen, A. 2000, *ApJ*, 531, L119

Aloy, M.A., Ibáñez, J.M., Miralles, J.A., & Urpin, V. 2002, *A&A*, 396, 693

Aloy, M.A., Martí, J.M., Gómez, J.L., Agudo, I., Müller, E., & Ibáñez, J.M. 2003, *ApJ*, 585, L109

Aloy M. A., Janka H.-T., Müller E., 2005, *A&A*, 436, 273

Aloy, M.A., & Rezzolla, L. 2006, *ApJ*, 640, L115

Aloy M. A., Obergaulinger, M., 2007, *Revista Mexicana de Astronomía y Astrofísica*, 30, 96

Attridge, J.M., Roberts, D.H., & Wardle, J.F.C. 1999, *ApJ*, 518, L87

Baan, W.A. 1980, *ApJ*, 239, 433

Begelman, M.C., Li, Z.-Y. 1994, *ApJ*, 426, 269

Birkinshaw, M. 1991, *MNRAS*, 252, 505

Birkl, R., Aloy, M. A., Janka, H. -Th., & Mueller, E. 2007, *A&A*, 463, 51

Blandford, R.G. 2002, in *ESO Astrophysics Symposia*. Eds. M. Gilfanov, R. Sunyaev, & E. Churazov. Springer-Verlag, p. 381

Blandford, R. 2003, *Ap&SS*, 288, 155

Blumenthal, G.R., Gould, R.J. 1970, Rev. Mod. Phys., 42, 237

Brown, G. L. & Roshko, A. 1974, J. Fluid Mech., 64(4), 775

Brunetti, G., Bondi, M., Comastri, A., Setti, G. 2001, A&A, 381, 795

Cawthorne, T.V., Wardle, J.F.C., Roberts, D.H., & Gabuzda, D.C. 1993, ApJ, 416, 519

Chiaberge, M., Celotti, A., Capetti, A., & Ghisellini, G. 2000, A&A, 358, 104

Crusius, A., & Schlickeiser, R. 1986, A&A, 164, L16

Dermer, C.D. 1995, ApJ, 446, L63

De Young, D. S. 1993, ApJ, 405, L13

Dulwich, F., Worrall, D.M., Birkinshaw, M., Padgett, C.A., Perlman, E.S. 2007, MNRAS, 374, 1216

Earl, J.A., Jokipii, J.R., Morfill, G. 1988, ApJ, 331, L91

Fendt, C. 2006, ApJ, 651, 272

Fendt, C., Ouyed, R. 2004, ApJ, 608, 378

Ferrari, A. 1998, ARA&A, 36, 539

Ferrari, A., Trussoni, E., & Zaninetti, L. 1978, A&A, 64, 43

Ferrari, A., Trussoni, E., & Zaninetti, L. 1982, MNRAS, 198, 1065

Hanasz, M., & Sol, H. 1996, A&A, 315, 355

Hardcastle, M.J., Alex&er, P., Pooley, G.G., & Riley, J.M. 1997, MNRAS, 288, L1

Hardcastle, M.J., Birkinshaw, M., & Worrall, D.M. 2001, MNRAS, 326, 1499

Hardcastle, M.J., Croston, J.H. 2005, MNRAS, 363, 649

Hardcastle, M.J., Kraft, R.P., Sivakoff, G.R., et al. 2007, ApJ, 670, L81

Hardee, P.E. 1979, ApJ, 234, 47

Hardee, P.E. 2007, ApJ, 664, 26

Kataoka, J., & Stawarz, L. 2005, ApJ, 622, 797

Kataoka, J., & Stawarz, L., Aharonian, F., Takahara, F., Ostrowski, M., Edwards, P.G. 2006, ApJ, 641, 158

Komissarov, S.S. 1990, SvAL, 16, 284

Laing, R.A. 1996, in ‘*Energy Transport in Radio Galaxies & Quasars*’, *ASP Conference Series vol. 100*, eds. P.E. Hardee, A.H. Bridle & J.A. Zensus, San Francisco

Leismann, T., Antón, L., Aloy, M. A., Müller, E., Martí, J. M., Miralles, J. A., Ibáñez, J. M. 2005, A&A, 436, 503

McKinney, J.C., Narayan, R. (2007), MNRAS, 375, 513

Melinani, Z., Keppens, R. 2007, A&A, 475, 785

Mimica P., Aloy M-A., Müller E., Brinkmann W. 2004, A&A, 418, 947

Mimica P., Aloy M-A., Müller E., Brinkmann W. 2005, A&A, 441, 103

Mimica P., Aloy M-A., Müller E. 2007, A&A, 466, 93

Mizuno, Y., Hardee, P., Hartmann, D.H., Nishikawa, K.-I., & Zhang, B. 2008, ApJ, 672, 72

Ostrowski, M. 1990, A&A, 238, 435

Ostrowski, M. 1998, A&A, 335, 134

Ostrowski, M. 2000, MNRAS, 312, 579

Owen, F.N., Hardee, P.E., & Cornwell, T.J. 1989, ApJ, 340, 698

Perlman, E.S., Biretta, J.A., Fang, Z., Sparks, W.B., & Macchetto, F.D. 1999, AJ, 117, 2185

Perucho, M., Hanasz, M., Martí, J. M., & Miralles, J. A. 2007, Phys. Rev. E, 75, 056312

Pudridtz, R.E., Rogers, C.S., Ouyed, R. 2006, MNRAS, 365, 1131

Rieger, F. M., & Duffy, P. 2004, ApJ, 617, 155

Romero, R., Martí, J.M., Pons, J.A., Ibáñez, J.M., Miralles, J.A. (2005), J. Fluid Mech. 544, 323

Siemiginowska, A., Bechtold, J., Aldcroft, T.L., Elvis, M., Harris, D.A., Dobrzycki, A. 2002, ApJ, 570, 543

Skibo, J.B., Dermer, C.D., Kinzer, R.L. 1994, ApJ, 426, L23

Stawarz, L., & Ostrowski, M. 2002, ApJ, 578, 763 (SO02)

Stawarz, L., Siemiginowska, A., Ostrowski, M., & Sikora, M. 2005, ApJ, 626, 120

Stawarz, L. 2007, private communication.

Swain, M.R., Bridle, A.H., & Baum, S.A. 1998, ApJ, 507, L29

Turland, B. D., & Scheuer, P. A. G. 1976, MNRAS, 176, 421

Urpin, V. 2002, A&A, 385, 14

Urpin, V. 2006, A&A, 455, 779

Wilson, A.S., Young, A.J., Shopbell, P.L. 2001, ApJ, 547, 740

Worrall, D.M., Birkinshaw, M., & Hardcastle, M.J. 2001, MNRAS, 326, L7

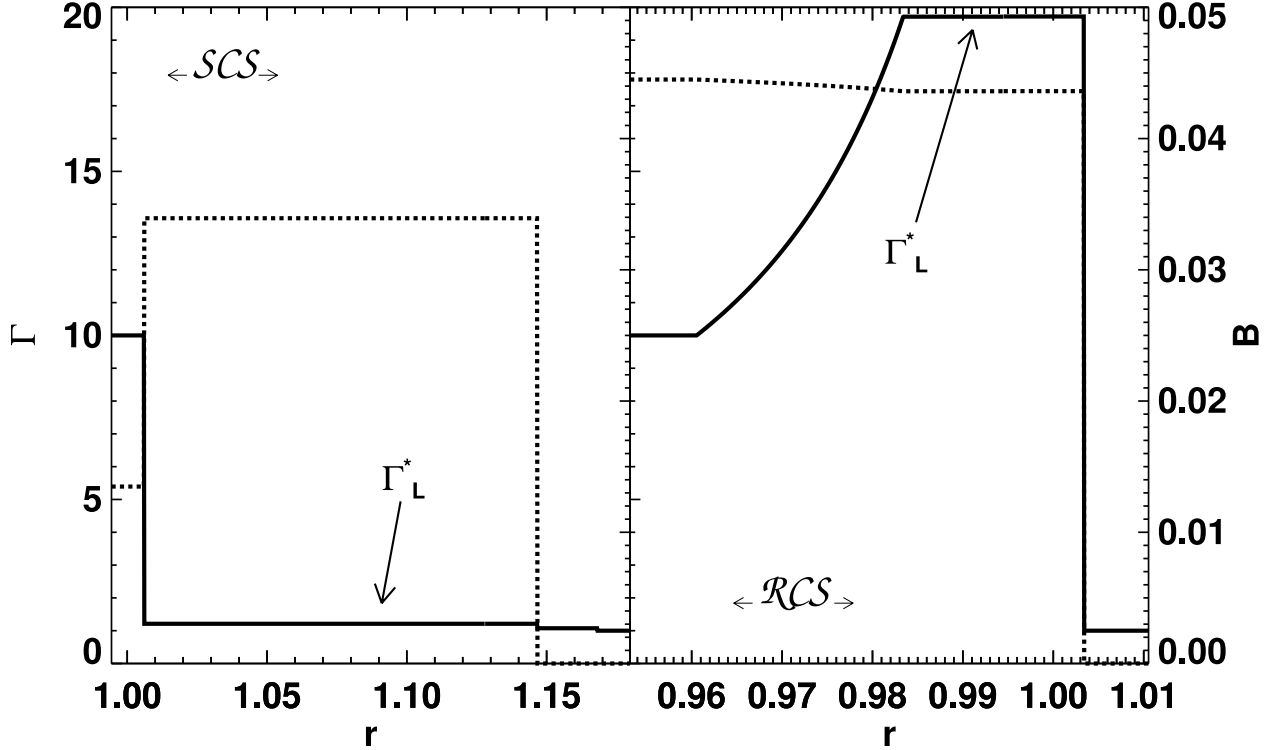


Fig. 1.— *Left panel:* Profiles of the Lorentz factor (solid line) and of the laboratory frame magnetic field (dashed line) resulting from a prototypical Riemann problem yielding a $\leftarrow SCS \rightarrow$ pattern. The initial left and right states are $(p_L, \rho_L, v_L^n, \Gamma_L, \tilde{\beta}_L) = (10^{-5}, 10^{-7}, 0.9, 10, 0.1)$ and $(p_R, \rho_R, v_R^n, \Gamma_R, \tilde{\beta}_R) = (10^{-6}, 10^{-2}, 0, 1, 0.1)$, respectively. Note that no boost is produced to the left of the contact discontinuity located at $r \simeq 1.147$. *Right panel:* Same as the left panel, but for a prototype $\leftarrow RCS \rightarrow$ pattern. The initial left and right states are $(p_L, \rho_L, v_L^n, \Gamma_L, \tilde{\beta}_L) = (10^{-5}, 10^{-7}, 0, 10, 100)$ and $(p_R, \rho_R, v_R^n, \Gamma_R, \tilde{\beta}_R) = (10^{-6}, 10^{-2}, 0, 1, 0.1)$, respectively. Note the boost (i.e., $\Gamma_L^* > \Gamma_L$) reached by the rarefied jet to the left of the contact discontinuity at $r \simeq 1.003$. In both cases the initial discontinuity is set at $r = 1$ and the solution is shown after an arbitrary amount of time (we recall that the solution of the Riemann problem is self-similar).

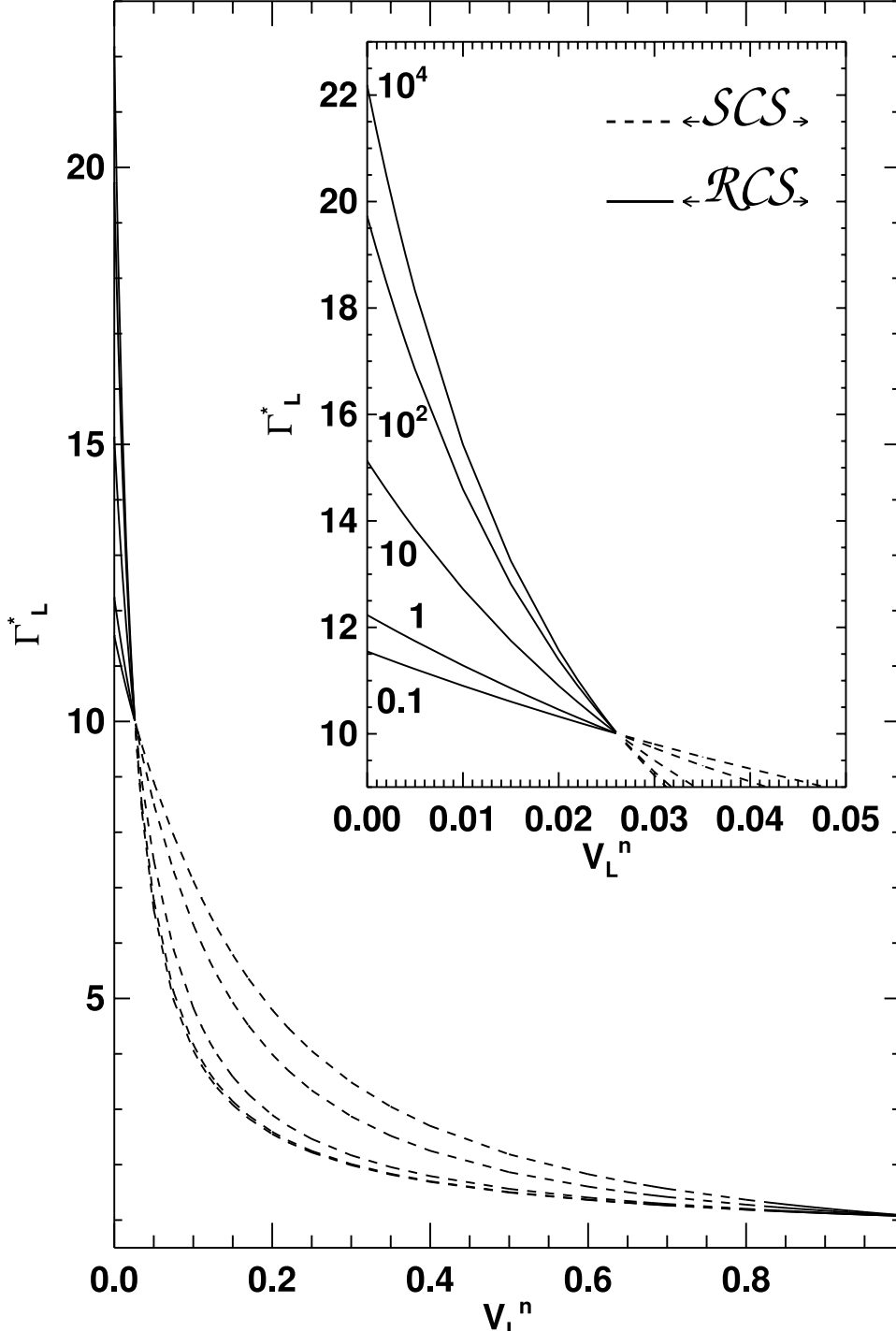


Fig. 2.— Lorentz factor reached at the uniform state left to the contact discontinuity Γ_L^* as a function of the normal velocity in the left state v_L^n . The right state is held fixed and is given by $(p_R, \rho_R, v_R^n, \Gamma_R, \tilde{\beta}_R) = (10^{-6}, 10^{-2}, 0, 1, 0.1)$. The left state has fixed values in the total pressure, the rest-mass density and the Lorentz Factor $(p_L, \rho_L, \Gamma_L) = (10^{-5}, 10^{-7}, 10)$, while the magnetization $\tilde{\beta}_L$ is varied for each curve as indicated by the different labels (see inset). The solid lines refer to the $\leftarrow \mathcal{RCS} \rightarrow$ pattern, and the dashed lines refer to a $\leftarrow \mathcal{SCS} \rightarrow$ pattern. The inset shows a zoom of the solutions for very small values of v_L^n , which are the most expected ones for *standard* jet flows.

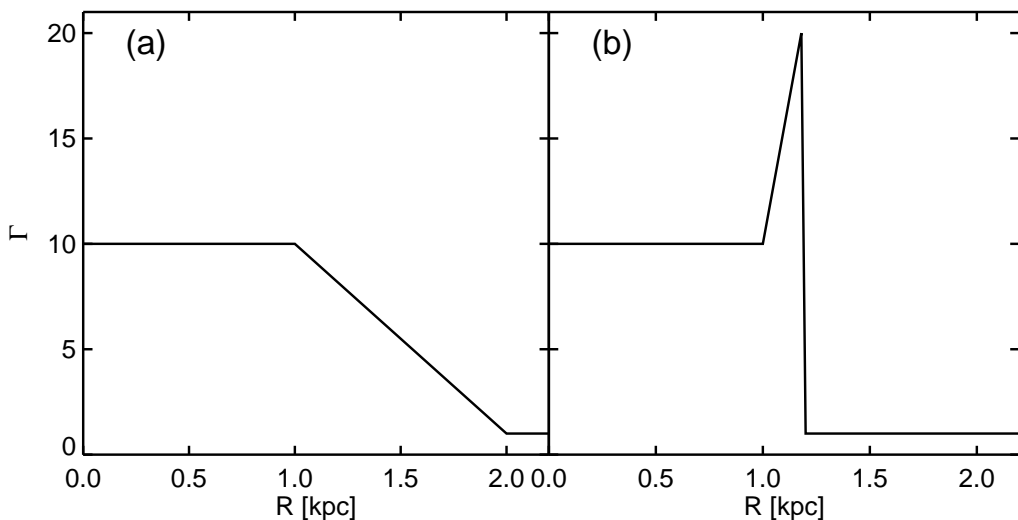


Fig. 3.— Radial profile of the Lorentz factor across the jet showing the kinematic difference in the structure of an standard, monotonic shear layer (panel a) and an anomalous shear layer structure (panel b).

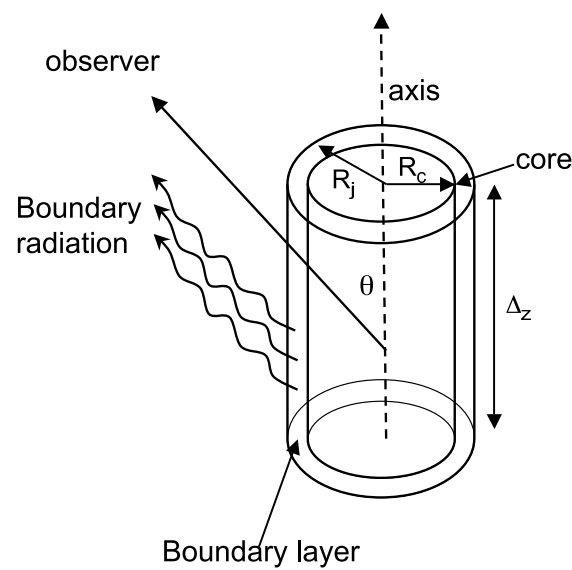


Fig. 4.— Schematic view of the jet model.

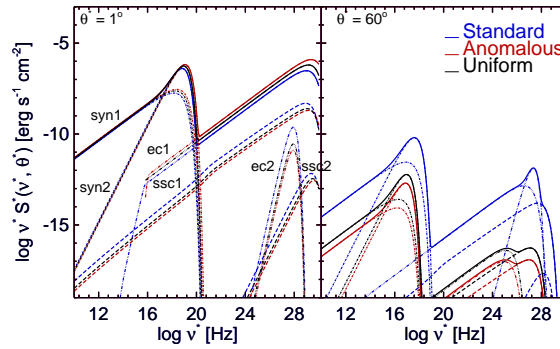


Fig. 5.— Predicted spectral energy distributions of the radiation generated in several boundary layers of a kpc-scale jet at $\theta^* = 1^\circ$ and $\theta^* = 60^\circ$ assuming $\gamma_{\text{eq}} = 10^8$. The blue lines corresponds to the same monotonic shear layer profile as in SO02, the black lines to a uniform boundary layer and the red lines to an anomalous one (see Sect. 3.2). The different contributions to the spectrum are labeled above the corresponding lines. The labels 1 and 2 refer to the components associated to the power-law and to the monoenergetic parts of the electron distribution (Eq. 2), respectively.

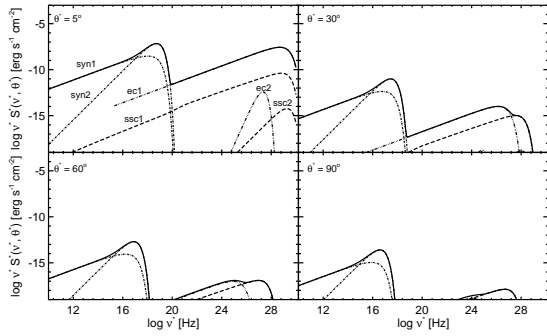


Fig. 6.— Predicted spectral energy distributions of the radiation generated by an AR boundary layer ($\Gamma_c = 10$, $\Gamma_{j,2} = 20$) of a kpc-scale jet assuming $\gamma_{eq} = 10^8$, for observing angles $\theta^* = 5^\circ, 30^\circ, 60^\circ$ and 90° . Indices 1 and 2 denote the spectral components associated to the power-law isotropic energy distribution and to the monoenergetic part, respectively. Absorption of VHE gamma-rays during the propagation to the observer is neglected.

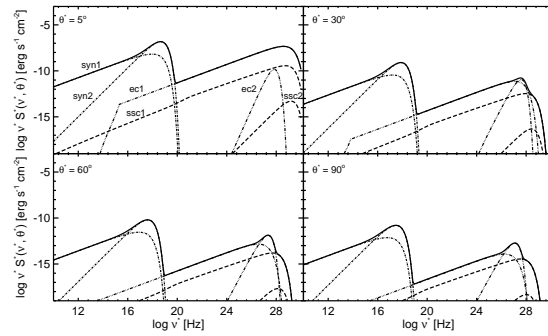


Fig. 7.— Same as Fig.6 but for a standard boundary layer ($\Gamma_c = 10$, $\Gamma_{j,1} = 1$).

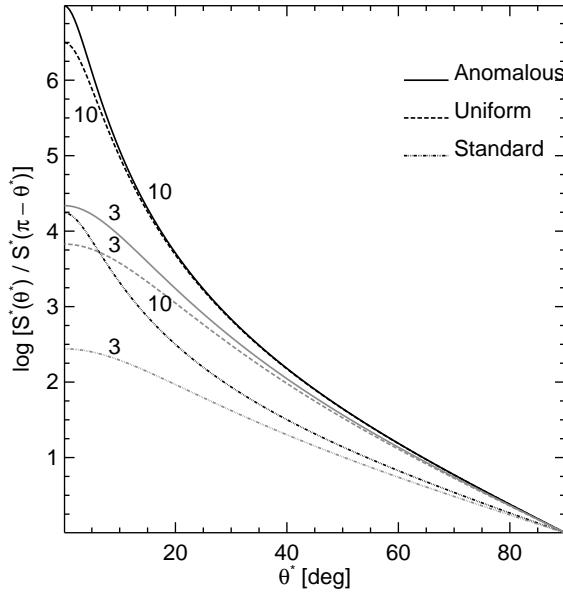


Fig. 8.— Jet-to-counterjet flux density ratio, $S^*(\theta^*)/S^*(\pi - \theta^*)$ at radio frequencies, as a function of the viewing angle θ^* . Black and grey lines correspond to values $\Gamma_c = 10$ and $\Gamma_c = 3$, respectively –the values of Γ_c are provided near the respective curves–. The black (grey) solid line corresponds to the radiation from an anomalous boundary shear layer with the radial profile of Eq. 14 and $\Gamma_{j,1} = 15$ ($\Gamma_{j,1} = 4.5$). The dashed-dotted line corresponds to the radiation from a monotonic boundary layer with the radial profile of Eq. 14 and $\Gamma_{j,2} = 1$. The dashed line corresponds to the model with a uniform boundary layer with a Lorentz factor $\Gamma_{j,3} = 10$.

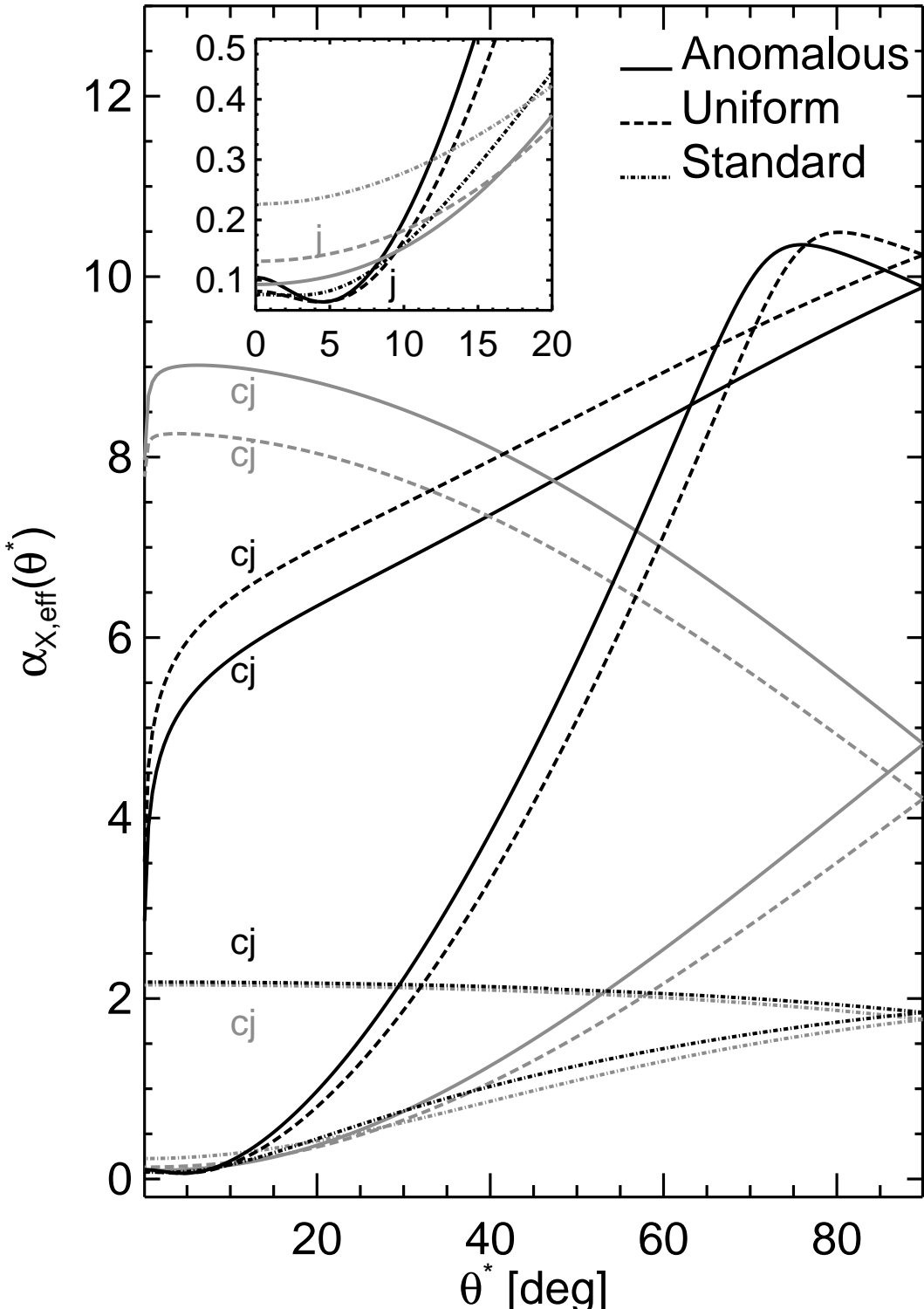


Fig. 9.— Expected effective X-ray spectral index of a jet (j) and of a counterjet (cj) boundary layer emission, $\alpha_{X,\text{eff}}(\theta^*)$, as a function of the viewing angle θ^* . Solid, dash-dotted and dashed lines correspond to jets with anomalous, standard and uniform shear layers, respectively (Eq. 14). Black (grey) lines correspond to jets whose core moves with a Lorentz factor $\Gamma_c = 10$ ($\Gamma_c = 3$). The inset shows a zoom of the jet $\alpha_{X,\text{eff}}$ for the smallest viewing angles θ^* .